HHS Public Access

Author manuscript

Acta Biomater. Author manuscript; available in PMC 2018 November 01.

Published in final edited form as:

Acta Biomater. 2017 November ; 63: 294–305. doi:10.1016/j.actbio.2017.09.007.

Three-Dimensional Nano-Architected Scaffolds with Tunable Stiffness for Efficient Bone Tissue Growth

Alessandro Maggi[1], **Hanqing Li**[2], and **Julia R. Greer**[1]

[1]Division of Engineering and Applied Science, California Institute of Technology, Pasadena CA, 91125, USA

[2]Division of Biology and Biological Engineering, California Institute of Technology, Pasadena CA, 91125, USA

Abstract

The precise mechanisms that lead to orthopedic implant failure are not well understood; it is believed that the micromechanical environment at the bone-implant interface regulates structural stability of an implant. In this work, we seek to understand how the 3D mechanical environment of an implant affects bone formation during early osteointegration. We employed two-photon lithography (TPL) direct laser writing to fabricate 3-dimensional rigid polymer scaffolds with tetrakaidecahedral periodic geometry, herewith referred to as nanolattices, whose strut dimensions were on the same order as osteoblasts' focal adhesions (~2μm) and pore sizes on the order of cell size, ~10μm. Some of these nanolattices were subsequently coated with thin conformal layers of Ti or W, and a final outer layer of 18nm-thick TiO_2 was deposited on all samples to ensure biocompatibility. Nanomechanical experiments on each type of nanolattice revealed the range of stiffnesses of 0.7–100 MPa.

Osteoblast-like cells (SAOS-2) were seeded on each nanolattice, and their mechanosensitve response was explored by tracking mineral secretions and intracellular f-actin and vinculin concentrations after 2, 8 and 12 days of cell culture in mineralization media.

Experiments revealed that the most compliant nanolattices had ~20% more intracellular f-actin and ~40% more Ca and P secreted onto them than the stiffer nanolattices, where such cellular response was virtually indistinguishable.

We constructed a simple phenomenological model that appears to capture the observed relation between scaffold stiffness and f-actin concentration. This model predicts a range of optimal scaffold stiffnesses for maximum f-actin concentration, which appears to be directly correlated with osteoblast-driven mineral deposition.

This work suggests that three-dimensional scaffolds with titania-coated surfaces may provide an optimal microenvironment for cell growth when their stiffness is similar to that of cartilage (~0.5–

3MPa). These findings help provide a greater understanding of osteoblast mechanosensitivity and may have profound implications in developing more effective and safer bone prostheses.

Graphical abstract

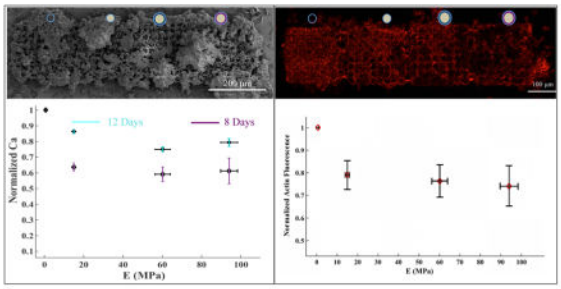

Creating prostheses that lead to optimal bone remodeling has been a challenge for more than two decades because of a lack of thorough knowledge of cell behavior in three-dimensional (3D) environments. Literature has shown that 2D substrate stiffness plays a significant role in determining cell behavior, however, limitations in fabrication techniques and difficulties in characterizing cell-scaffold interactions have limited our understanding of how 3D scaffolds' stiffness affects cell response.

The present study shows that scaffold structural stiffness affects osteoblasts cellular response. Specifically this work shows that the cells grown on the most compliant nanolattices with a stiffness of 0.7MPa expressed ~20% higher concentration of intracellular f-actin and secreted ~40% more Ca and P compared with all other nanolattices. This suggests that bone scaffolds with a stiffness close to that of cartilage may serve as optimal 3D scaffolds for new synthetic bone graft materials.

Introduction

The number of expected osteoporosis-related fractures is predicted to grow by a factor of 7 in the next twenty-five years because of a substantial increase in the ageing population. By 2030, the demand for hip and knee replacements is predicted to increase by 174% and 673%, respectively[1]. This tremendous need for bone prostheses has motivated significant research efforts to develop a more thorough understanding of properties of bone at each level of its hierarchy, with a focus on scaffold-osteoblast interactions at the cellular level[2,3]. Several types of bone grafting scaffolds exist. For example, autografts are bone replacements taken directly from the iliac crest of a patient and transplanted to the target site where they lead to osteointegration, osteoinduction and osteogenesis, which are necessary for a functional bone implant.

Autografts virtually eliminate the risk of implant rejection but they suffer from donor site morbidity and there is limited graft availability. Significant efforts have been directed at developing fully synthetic implants for more than five decades[2]. Commercially available, fully synthetic orthopedic implants are primarily manufactured out of stainless steel and titanium alloys to achieve the required fatigue strength, high strength-to-weight ratio,

flexibility, resistance to corrosion, and biocompatibility[3]. The stiffness of these materials is at least two orders of magnitude greater than that of cancellous bone, 0.04 – 1 GPa[4]. This discrepancy in stiffness between bone and the implant results in insufficient mechanical load transfer from the implant to the surrounding tissues, which leads to a phenomenon known as stress shielding. The bone adapts to these reduced stresses, relative to its natural state, by decreasing its mass, which prevents the bone from anchoring to the implant and leads to implant loosening and eventual failure.[4–7] Hutmacher et al. postulated that an ideal implant should retain durability in the body and have mechanical properties that match those of the natural bone that is being replaced[5]. This remains to be demonstrated experimentally, especially at the cellular level.

To date, research on mammalian cells' ability to exert forces onto a 2-dimensional substrate via stress fibers, which are bundles of polymerized actin, has shown that cells exhibit a bell-shaped sensitivity to changes in substrate stiffness[8,9]. We hypothesize that adhesion and mineralization behavior of bone cells may also exhibit a sensitivity dependence on the stiffness of 3-dimensional (3D) scaffolds[8,10,11,12]. Identifying an optimal stiffness range for mineralization on 3D scaffolds has the potential to offer quantitative guidelines for the fabrication of bone implants that minimize stress-shielding while maximizing bone growth.

Challenges associated with fabricating complex three-dimensional scaffolds with strut dimensions on the same order as osteoblasts (~10μm) has rendered existing studies to be limited to a stiffness window ranging from ~10–200 kPa[13–16]. Most literature has been focused on studying cell behavior on either 2D substrates or on scaffolds with a narrow range of structural stiffness and strut size of at least one order of magnitude larger than the cell's size which has made the cell-scaffold interaction virtually the same as that on a 2D substrate [5,13,15–19].

3D porous scaffolds with different pore sizes have been shown to offer an excellent platform to mimic natural physiologically relevant microenvironments[18,20,21]. For example, Raimondi et al. fabricated polymeric scaffolds and observed that a minimum pore size of 10μm was necessary to allow for cell infiltration into their scaffold[18]. Tayalia et al. utilized polymeric scaffolds and showed that cells are more uniformly dispersed inside scaffolds with pore sizes of 52μm compared to 12μm[21]. Harley et al. produced collagen–glycosaminoglycan scaffolds and showed that cell migration and cell speed increased by a factor of 2 when the scaffold's pore size was reduced from 151 to 96 μm[20,22–24]. Most of these studies focused on investigating the relationship between porosity and cellular behavior, with some discussing cell behavior as a function of scaffold stiffness, which likely serves as a key factor in governing osteoblasts' mineralization abilities[25].

We focus on exploring the dependence of osteoblast-like cells (SAOS-2) on the structural stiffness of porous substrates with a constant pore size. We utilized two-photon lithography, sputtering and atomic layer deposition (ALD) to fabricate periodic, 3-dimensional cellular solids, referred to as nanolattices, with tetrakaidecahedral geometry, measured their structural stiffness, and populated osteoblast-like SAOS-2 cells onto them to study their behavior. The structural modulus of elasticity, or stiffness, E^*, scales with the relative density, $\bar{\rho}$, of a periodic cellular solid, as:

$$E^* = C E_s (\bar{\rho})^m \quad (1)$$

where C is a geometry-dependent proportionality constant, E_s is the elastic modulus of the solid that comprises the solid[26,27] and m is a topology-dependent power law coefficient. The relative density is defined as the volume fraction of the solid material, V_s, divided by the representative volume of the unit cell, V_{uc} [28,29]:

$$\bar{\rho} = \frac{V_S}{V_{UC}} \quad (2)$$

Relative density is a function of unit cell topology, mean pore size, U, and the ratio of beam-length to beam-radius, L/R, as shown in Fig. 1(i). The relative density of the nanolattices in this work, calculated using Solidworks software (Dassault Systems), ranged from 0.14% to 12.2%.

The pore size, U, was maintained constant at 25μm for all nanolattices in this work to isolate the effects of the scaffolds' structural stiffness, which was varied by depositing different material coatings onto the original polymer nanolattices (Fig. 1). We were able to achieve a range of structural stiffnesses that spans over two orders of magnitude, from ~0.7 MPa to 100 MPa, which covers a region that had not been previously explored: existing literature on scaffolds with similar sizes explored the stiffness range of ~10–200 kPa.

SAOS-2 cells were seeded on the nanolattices, and the cells' f-actin concentration was measured after a 48-hour growth period in mineralization media. Longer periods of growth, up to 12 days, were conducted to characterize the relationship between scaffold stiffness and cells' mineralization ability.

2. Materials and Methods

2.1. Sample preparation

All scaffolds were fabricated via TPL direct laser writing (DWL), which employs a femtosecond-pulsed laser that is rastered in space to selectively cross-link a negative tone photoresist, IP-Dip (Nanoscribe GmbH), into a designed structure. The resulting polymer nanolattices were subsequently coated with different materials to create scaffolds that are comprised of 4 different material systems shown in Fig. 1(i).

Material system (A) was fabricated by first coating the polymer scaffold with an 18nm-thick layer of TiO_2 deposited via ALD and then slicing off the sample edges along each face using a focused ion beam (FIB) (FEI Nova 200 Nanolab) at 30KeV and 5nA. The samples were then placed into an O_2 plasma etcher at 0.6 mbarr and 100W (Diener GmbH) for 24 hours to etch away the original scaffold and to produce a hollow TiO2 nanolattice (Fig. 1(ii), 1(iv)). **Material system (B)** was fabricated using the same process as Material system (A) without etching away the polymer scaffold. **Material system (C)** was fabricated by sputtering a ~250nm-thick layer of Ti onto the original polymer scaffold and subsequently

coating it with an 18nm-thick layer of TiO_2 deposited via ALD. **Material system (D)** was fabricated by sputtering a ~250nm-thick layer of W onto the original polymer scaffold and subsequently coating it with an 18nm-thick layer of TiO_2 deposited via ALD.

Some of the original polymer nanolattices were used for fluorescence studies, which revealed the need to treat the polymer nanolattices with Sudan Black to suppress autofluorescence according to the protocol developed by Jaafar et al.[30] (supplementary information, Fig. S1).

Sputter deposition was carried out using a magnetron sputterer (Temescal BJD-1800). Titanium was sputtered using RF power at 125W, a working pressure of 6mtorr, Ar pressure of 60sccm and table rotation set at 100%. An average Ti thickness of ~250nm was obtained after depositing for 140 minutes. W was deposited using RF power of 125W, a working pressure of 5mtorr, Ar pressure of 50sccm and table rotation set at 100%. An average W thickness of ~250nm was obtained after depositing for 140 minutes. The outermost 18nm-thick TiO_2 coating was deposited using ALD (Cambridge Nanotech S200) with H_2O and Titanium Tetrachloride ($TiCl_4$) precursors. A shadow mask was used to selectively coat Ti on system (C) and W on system (D) that are adjacent to each other on the SiO_2 substrate (see supplementary material for details). Fig. 1(iii) provides a map generated by energy dispersive spectroscopy (EDS) that shows the distribution of Ti and W in material systems (C) and (D). The spraying effect inherent to sputtering deposition was minimized to ~15μm by reducing the size of the shadow mask's deposition window to 120μm × 120μm.

To mimic the porous structure of cancellous bone we chose a tessellated tetrakaidecahedral unit cell geometry (Fig. 1(i)) which had circular beams of length L = 8.33μm and a radius R = 1μm for material system (A) and (B) or R = 1.5μm for material systems (C) and (D), and a unit cell size U = 25μm for all material systems (Fig. 1(i)). Each nanolattice contained 8 (length) x 8 (width) x 2 (height) unit cells, and each sample contained 4 nanolattices arranged in a linear sequence from material system (A) to (D) to establish a stiffness gradient (Fig. 1(ii)). The nanolattices were separated by 10μm to allow for precise and selective sputter coating (Fig. 1(iii)).

2.3. Nanomechanical Experiments

All nanolattices were uniaxially compressed to a maximum strain of 50% at a strain rate of 10^{-3} s^{-1} in •a nanoindenter (G200, Agilent Technologies). The load vs. displacement data collected by the nanoindenter was converted into engineering stress vs. strain. Engineering stress was calculated using $\sigma = F/A$, where F is the applied load and A is the footprint area of the nanolattice, and global compressive strain, ε, was calculated as $\varepsilon = (H_f - H_i)/H_i$ where H_i is the initial height of the nanolattice measured from SEM images and $(H_f - H_i)$ is the displacement recordered by the nanoindenter. The structural stiffness of the nanolattice, E^*, was calculated as the slope of the elastic loading portion of the data, which is indicated by the dashed black line in Fig. 2(ii):

$$E^* = \frac{d\sigma}{d\varepsilon} \quad (3)$$

2.3. Cell Culture

All in vitro experiments were performed using the SAOS-2 cell line from ATCC. Cells were cultured in 100 mm dishes. DMEM, supplemented with 10% fetal bovine serum (FBS), 2mM L-glutamine, 100 U ml^{-1} penicillin and 100 μg ml^{-1} streptomycin, were used as the culture media. Media was replaced every 2 days, and cells were split every 4–5 days using Accutase Cell Detachment Solution. Differentiation media consisted of DMEM low glucose, with 10% FBS, 2mM L-glutamine, 100 U ml^{-1} penicillin and 100 μg ml^{-1} streptomycin, 10 mM - glycerophosphate, 100 nM dexamethasone, and 50 μM ascorbic acid.

For immunostaining experiments (subset 1), cells were seeded onto the nanolattices from each material system at a density of 12,000 cells/cm^{-2} and grown for 7 days, after which they were transferred into mineralization media and cultured for additional 2 days. Samples were then washed three times with PBS and fixed with 4% paraformaldehyde for 15 minutes. Samples were washed again with PBS and blocked with 1% BSA in PBS for 30 minutes. Anti-vinculin diluted in blocking buffer was then added to the cells and incubated overnight at 4°C, and samples were washed three times again with PBST incubated with phalloidin-555 and a 647-conjugated secondary antibody at room temperature for three hours. After the final wash with PBST, the cells were imaged with a confocal microscope (Zeiss LSM 710).

For mineralization experiments (subset 2), cells were seeded onto different nanolattices from each material system at a density of 12,000 cells/cm^{-2} and allowed to proliferate for 14 days. Cells were then transferred into mineralization media and cultured for additional 8 or 12 days. These samples were also washed three times in PBS and fixed in 4% paraformaldehyde for 15 min. After fixation, and one more wash with PBS, the cells were incubated in serial dilutions of ethanol for 10 minutes each.

2.5. Cell imaging and Secretions Characterization

After the cells from subset 1 were grown on the nanolattices for 2 days in mineralization media, they were imaged to quantify the amount of fluorescence from f-actin and vinculin staining. Samples were imaged in a Zeiss LSM 710 confocal microscope using a 20x, NA 0.8 lens, which offered the highest magnification to image the entire nanolattice. Z-stack images were captured at a constant spacing of 1μm and a total height of 55μm and were used to calculate the maximum projected intensity using software ImageJ. To quantify the relative amount of fluorescence from every material system, fluorescence data from each individual chip was normalized by the fluorescence intensity of material system (A). A total of 5 chips were used to determine error in fluorescence experiments.

To quantify their propensity for mineralization, SAOS-2 cells from subset 2 were subjected to serial dilutions of ethanol in phosphate buffered saline until 100% ethanol was attained and then processed in a critical point dryer (Tousimis 915B). Cell secretions were morphologically and spectroscopically analyzed using a scanning electron microscope (SEM, FEI Nova 200 Nanolab) equipped with an EDS module (EDAX Genesis 7000). EDS parameters were adopted from Maggi et al.[19], and 3 scans per nanolattice were taken to ensure current stability. Raman analysis of cell secretions deposited onto the nanolattices

was carried out using a micro Raman spectrometer (Renishaw M1000) with a laser wavelength of 514.5 nm and a power density of 130W/cm^2.

2.6. Statistical Analysis

All cell fluorescence experiments were run in 5 replicates. Each sample contained all four material systems, and all fluorescence intensity measurements were normalized by that of the most compliant material system (A). This process was repeated for all 5 samples. Fluorescence intensity results were expressed as the mean fluorescence for each material collected from these 5 samples. The error was obtained by calculating the standard error for each material system.

All EDS experiments were run in triplicate. Similarly to the fluorescence analysis, the x-ray signal intensity was normalized by that of the most compliant material system (A). The error was obtained by calculating the standard error for each material system.

Compression experiments were performed in 4 replicates for each material system to determine the elastic modulus and compressive strength for each material system. Elastic modulus and compressive strength results were expressed as the mean of 4 compression tests and standard deviation was used to calculate the error associated with the measurements that were taken.

3. Results

3.1. Nanomechanical Experiments

We performed quasi-static uniaxial compression experiments to ~50% global uniaxial strain to determine the effective structural stiffness and deformation characteristics of each nanolattice. Fig. 2 shows SEM images of nanolattices from each material system before and after the compression, as well as the corresponding stress vs. strain data.

The stress-strain data for all samples contains a short initial non-linearity, or toe region, which is primarily caused by a small misalignment between the compression tip and the top surface of the nanolattice. The stiffer material systems (C) (polymer/Ti/TiO_2) and (D) (polymer/W/TiO_2) exhibited a toe region up to 1% strain; the toe region in more compliant systems (B) (polymer/TiO_2) and (A) (hollow/TiO_2) extended to 3% strain. A linear elastic region, indicated by the dashed slopes in Fig. 2(ii), followed the toe region, and was used to calculate the effective structural stiffness, E^* [31,32]. The post-elastic behavior varied depending on the constituent material of the nanolattice. Fig. 2(iii), which shows post-compression SEM images of a representative nanolattice from each material system, reveals that all the composite systems (B, C, and D) experienced catastrophic brittle failure at a strain of ~9%, ~13% and ~18% respectively; the hollow material system (A) deformed in a ductile-like fashion with discrete serrations that correspond to individual layer buckling events (Fig. 2(ii)-inset). Table I summarizes the moduli, E^*, and compressive strengths, σ_f, for all material systems, which span more than two orders of magnitude.

3.2. Cell experiments: f-actin & vinculin fluorescence microscopy

SAOS-2 cells were cultured on the nanolattices to determine the effect of substrate stiffness on the production of stress fibers and focal adhesions by the cells. After 2 days of growth in mineralization media, the actin fibers (f-actin) were stained with phalloidin (red) and the focal adhesions were stained with anti-vinculin antibodies (green) to quantify their amounts via fluorescent experiments (Fig. 3).

Fig. 3 shows the results of the fluorescence experiments. A schematic representation of each individual material system is placed directly above the image that was generated via fluorescence microscopy for that specific material system (Fig. 3(i–ii)). Fig. 3(iii) reveals the presence of ~20% more f-actin on the most compliant nanolattice (A) compared to that on the other material systems (B–D), all of which displayed similar levels of relative maximum intensity of f-actin. Fig. 3(iv) shows vinculin staining, which revealed no significant differences in focal adhesion concentration across the four material systems.

Merging the signal from phalloidin (Fig. 3(i)) and vinculin staining (Fig. 3(ii)) produced the images in Fig. 3(v), which show the amount of co-localization (yellow color) between f-actin and focal adhesions in the nanolattices. These images reveal uniform distribution of co-localized f-actin and focal adhesions along the z-axis with no apparent location preference within the nanolattice. A qualitative analysis also revealed higher levels of co-localization on the nanolattices compared to the flat substrate (Fig. 3(v)). The footprint area of the nanolattices occupied ~0.2% of the total sample area which made it impossible to physically separate the cells attached to the nanolattices from those on the neighboring flat substrate and to perform more quantitative biological assays.

Sudan Black was not able to suppress the inherent autofluorescence of the nanolattice polymer at wavelengths shorter than ~400nm, which rendered nuclear staining, such as DAPI, ineffective in revealing meaningful information about the number of cells on each nanolattice.

3.3. Cell experiments: cellular secretions characterization & quantification

Fig. 4 shows SEM images of SAOS-2 secretions on the nanolattices after a growth period of 8 and 12 days in mineralization media.

These experiments reveal that SAOS-2 cells deposited organic and mineral compounds on all nanolattices after growing in mineralization media for 8 and 12 days. SEM images in Fig. 4(i–vi) demonstrate the presence of a continuous matrix interspersed with ~50–100nm-diameter filaments that are indicated by arrows in Fig. 4(iii, iv, viii). The mineral deposits, indicated by arrows in Fig. 4(v, vi, ix), appear to have two dominant morphologies: (1) spherical clusters with diameters of ~2–15μm (Fig. 4(v, vi)) that are composed of (2) smaller aggregates ranging from ~300nm–1μm (Fig. 4(ix)). These smaller aggregates were also present as a continuous coating on the nanolattice beams (see supplementary information for more details).

Raman spectroscopy performed on the organic phase revealed peaks at 854 cm^{-1} and 879 cm^{-1}, which most probably correspond to proline and hydroxyproline, respectively, and

suggest the presence of collagen molecules. The spectra taken from the mineral phase exhibited a peak at 962cm^{-1} (Fig. 4(vii)), which is likely representative of some form of bioapatite.

Fig. 5 shows the results of the EDS analysis performed on the scaffolds after 8 and 12 days of cell growth in mineralization media. Nanolattices made from all material systems revealed the presence of C, O, Na, Mg, Ca and P.

EDS spectra of all samples after 8 days of growth reveal the relative intensity of C to be a factor of ~3 higher than those of P and Ca (Fig. 5(i)). EDS spectra after 12 days of growth reveal the amount of C to be ~6% lower than that of P and ~29% higher than that of Ca in all samples (Fig. 5(ii)). Fig. 5(iii–vi) displays the relative intensity of Ca and P after 8 and 12 days of cell growth as a function of nanolattice stiffness. The data from each sample was normalized to the corresponding element intensity on the most compliant material system (A). The intrinsic inability of EDS detectors to reliably capture light elements ($Z < 11$) limits the accuracy of quantifying the concentration of C. This analysis reveals that after 8 days, the hollow, most compliant material system (A) had ~40% more Ca and P compared with those on stiffer material systems (B–D), all of which displayed similar levels of Ca and P (Fig. 5(iii, v)). After 12 days, a less drastic difference in Ca and P concentration across the material systems was observed. Material system (A) displayed ~15% more Ca and P compared with material system (B), and material system (B) displayed ~10% more Ca and P than material systems (C) and (D) (Fig. 5(iv, vi)). These results show that material system (A) with the lowest structural modulus of 700kPa, had the highest amounts of f-actin and mineral deposits (Ca, P).

4. Phenomenological Model

To explain the observed higher cellular activity on the most compliant 3D substrates, we propose a simple qualitative phenomenological model that is aimed to relate f-actin concentration to substrate stiffness. The ability of a cell to respond to external mechanical stimuli depends on highly interconnected and coordinated networks of signaling events that regulate cell adhesion. Mammalian cells attach to a substrate by reorganizing their cytoskeleton, which is a complex, highly heterogeneous and dynamic system that undergoes constant rearrangement. Multiple components play important roles in cystoskeleton rearrangement. Following the approach of Ingber (1997)[33], in this model we treat the cytoskeleton as a network of microfilaments and microtubules that distribute forces within the cell through a balance of compression and tension without taking into account more detailed structures[33]. We setup the model by employing the following elements involved in cell adhesion: (1) a “sticky” element, focal adhesions, (2) an active force-generating element, f-actin, and (3) a compression element, microtubules.

Focal adhesions, which induce monomeric actin (g-actin) to polymerize into f-actin that can autonomously contract, are the anchor points of the cell to the substrate. F-actin pulls on the substrate by using integrins, or transmembrane proteins that serve as adhesive elements between the substrate and the cell. Rod-like protein complexes, or microtubules, resist this actin-driven cell and prevent cell collapse[34,35].

Existing models treat actin filaments and microtubules as linear-elastic solids, which predict a linear relationship between f-actin concentration and substrate stiffness[36,37]. This linear relationship saturates when the maximum biologically-allowed concentration of filamentous actin in the cell is reached (~60uM)[38]. These models accurately describe the interactions between f-actin and microtubules and do not account for the integrins, which play an important role in cell attachment and migration[34].

Following the approach of De Santis, et al.[39], who treated the cellular mechanical elements, f-actin and microtubules, as linear elastic springs, we developed a model that accounts for the f-actin-integrin-substrate interaction. In this model, the cells are in quasi-static equilibrium with the substrate, and the force generated by the filamentous actin (F_{FA}), which is a function of the force developed in the integrins (F_{IT}), is balanced by the compression of the microtubules (F_{MT}), and the traction at the cell-substrate interface (F_S) (Fig. 6(i)).

To satisfy static equilibrium, the following relation must be true:

$$F_{MT}+F_{FA}+F_S=0 \quad (4)$$

Each force can be expressed in terms of spring constants and dimensions as:

$$\begin{aligned} F_{FA}&=K_{FA}(L-L_{FAR})/L_{FAR} \\ F_{MT}&=K_{MT}(L-L_0)/L_{FAR} \\ F_S&=K_S(L-L_0)/L_0 \end{aligned} \quad (5)$$

where L_0 is the rest length of an element, L is the final elongation of an element, and $K = EA$ is the effective spring constant of the element where E is the Young's modulus of the element, and A is the cross sectional of the element. K_{FA} is the effective stiffness of f-actin, K_{MT} is the effective stiffness of microtubules and K_S is the effective stiffness of the substrate.

The rest lengths of the microtubule and of the substrate are independent of a cell's pre-stress[39], the f-actin rest length (L_{FAR}) is a function of the pre-stress developed by a cell upon its adhesion to a substrate[40]:

$$L_{FAR}=(1+P)L_0 \quad (6)$$

where P is a unitless pre-stress coefficient which we estimated using Engler et al.[8] Solving equations (5) and (6) gives an expression for the force that f-actin exerts onto the substrate as a function of its stiffness:

$$F_{FA}=\frac{K_{FA}P(K_{MT}+K_S)}{K_{FA}+(K_{MT}+K_S)(1+P)} \quad (7)$$

Eq. (8) doesn't take into account the integrins, which play a crucial role in cell mechanics. Li et al. showed that a single integrin-substrate bond has a strength of ~100pN. Once the force exerted by the contracting f-actin exceeds this strength, the integrins dissociate from the substrate[41]. Following the approach of Li et al. and He et al.[37], we modeled the probability of an integrin-substrate bond rupture (Pi_R) as a function of actin-generated tension. We then calculated the cumulative distribution function (CDF) for 4000 integrins (Fig. 6(ii)), which literature has shown to be a reasonable average number of integrins per μm^2 [42].

$$CDF(Pi_R) = \frac{1}{2}\int (Pi_R) dF_{FA} \quad (8)$$

We incorporated the effects of integrin-substrate bonds rupturing on the effective force exerted by f-actin by modeling integrins as sliders that work in series with the actin filaments, as shown in Fig. 6(i). Multiplying Eq. (7), which represents the linear relationship between actin force and substrate stiffness, by the probability of finding an intact integrin-substrate bond gives the f-actin activation factor, η_{FA}:

$$\eta_{FA} = \frac{\frac{K_{FA}P(K_{MT}+K_S)}{K_{FA}+(K_{MT}+K_S)(1+P)}(1-CDF(Pi_R))}{F_{FA(\max)}} \quad (9)$$

η_{FA} describes the change in f-actin concentration relative to the baseline level of 0, which corresponds to the minimum amount of polymerized actin necessary for the cell to remain attached to a substrate, to a maximum level of 1, which corresponds to the highest possible effective concentration of f-actin in the cell.

Eq. (9) demonstrates that η_{FA} is related to the probability of integrins dissociating from the substrate, which is a function of the force that f-actin exerts (Eq. 8) that is related to the substrate stiffness, K_s, as shown in Eq. (8). η_{FA} was normalized by the maximum force that f-actin can exert, which is dictated by the maximum concentration of actin allowed by the cell.

Fig. 6(iii) shows a plot of η_{FA} as a function of the substrate modulus ($E_s = K_s/A$) predicted by the model, which reveals a linear increase in actin activation with substrate stiffness up to ~2MPa where the role of integrin dissociation becomes dominant. The maximum f-actin activation occurs at the substrate stiffness of 2.3 MPa where about 20% of the integrin-substrate bonds have broken (Fig. 6(ii)). As more integrin-substrate bonds dissociate, η_{FA} rapidly decreases back to the baseline level of 0 at the substrate stiffness of 5.2 MPa, where virtually 100% of the integrin-substrate bonds have broken and only the baseline integrin-substrate bonds, essential for the cell-substrate attachment, remain.

The model predicts a specific range of substrate stiffnesses, 0–2.5MPa, where the f-actin activation factor rises from 0 to 1 and then rapidly decays back to the baseline level for all

higher stiffnesses. In reality, the rise and decay of η_{FA} would probably be more gradual because of the dynamic nature of integrin-substrate bond kinetics. This simple model is not able to capture the kinetics of the integrin-substrate bonds and is formulated based on the steady state approximation.

To evaluate the credibility of the proposed model, we fabricated an additional material system, a polymer skeleton with a tetrakaidecahedral unit cell, pore size $U = 25\mu m$, beam radius of 0.5 μm coated with an 18-nm-thick TiO_2 layer, whose structural stiffness was measured to be ~3MPa, i.e. within the range of non-zero η_{FA}.

We conducted the same fluorescence experiments by growing SAOS-2 cells on the nanolattices for 2 days in mineralization media, staining for actin fibers and measuring the f-actin fluorescence intensity which represents the degree of f-actin activation (see supplementary information for more details). Figure 6(iv) shows the experimentally obtained f-actin fluorescence data plotted together with the model predictions. It appears that the proposed phenomenological framework that is based on coupling the probability of integrins dissociating from the substrate to the existing linear elastic models for cell mechanics accurately captures the experimental observations in the range of stiffnesses studied, 0.7 to 100MPa.

5. Discussion

The global need for more effective osteogenic scaffolds has motivated a debate on the optimal scaffold specifications, especially about the mechanical properties like scaffold stiffness and strength[15]. At the macroscale, it has been shown that implants with elastic moduli on the order of hundreds of GPa cause stress shielding, which hinders long-term bone healing[6]. The fundamental causes of stress shielding likely originate at the microscale and remain largely unknown. This work aims to quantify the effects of structural stiffness of 3-dimensional nano-architected scaffolds on the stress distribution and mineralization capability of osteoblast-like cells (SAOS-2).

5.1. Mechanical characterization

A relatively large span of relative densities, 0.14%–12.2%, coupled with a tetrakaidecahedral open cellular architecture and different thin film coatings enabled us to fabricate 3-dimensional scaffolds that spanned more than two orders of magnitude in structural stiffness, ~0.7–100 MPa. The mechanical behavior of the nanolattices was analyzed via quasi-static uniaxial compression experiments, which revealed two distinct deformation behaviors: global brittle failure exhibited by composite material systems (B), (C) and (D), and layer-by-layer collapse exhibited by hollow material system (A). A toe region was present in all compressions up to ~3% strain and was likely caused by: (1) a slight initial misalignment between the 600μm–diameter compression tip and the 200μm–wide nanolattice and (2) the incomplete initial contact caused by the fabrication-induced concavity of the top nanolattice surface (see supplementary material, Fig. S5, for more details.) Following the toe region, nanolattices made from material system (A) (hollow TiO_2 nanolattice with 18nm wall thickness) underwent linear elastic loading up to 5% strain and a stress of 12 kPa, followed by a series of discrete strain bursts that correspond to the individual beam buckling events,

which ultimately led to brittle fracture of the TiO_2 beam wall[43]. The initial strain burst was always the most extensive, ~10%, all subsequent strain bursts were ≤ 5%. This is likely a result of the substantial accumulation of strain energy in the fully intact sample during loading until its release in the first instability/buckling event, after which the weakened nanolattice is not capable of sustaining as much strain energy between each layer collapse.

Material system (B) (polymer scaffold coated with 18nm of TiO_2) displayed linear-elastic behavior up to 3% strain and ~0.3MPa stress. Inelastic deformation commenced at stresses higher than ~0.3 MPa, which generated high tensile, so-called “hoop”, stresses in the outer TiO_2 shell at the nodal connections of the nanolattice and caused brittle fracture of the entire beams and nodes and led to catastrophic collapse of the entire nanolattice[44,45]. Material system (C) (polymer-Ti-TiO_2) and (D) (polymer-W-TiO_2), each containing 26% metal by volume, exhibited similar mechanical behavior characterized by an initial linear elastic response up to ~5% strain followed by yielding and limited plasticity of the composite beams. Global brittle failure occurred at a compressive stress of ~3 MPa for material system (C) and at ~8 MPa for material system (D) because the latter is ~1.5 times stiffer. The ensuing structural collapse occurred because of inefficient load re-distribution within the nanolattice after fracture of the individual nodes and beams, which disabled the nanolattice to be capable of carrying the applied compressive load.

5.2 Cell Response: f-actin and vinculin distribution

Physical cues, such as substrate stiffness, are known to affect cellular stress states, which activate pathways that control cell behavior[10]. Studies have shown that stem cell differentiation fate has a bell-shaped dependency on substrate stiffness[8]. For example, stem cells grown on compliant 2D substrates (0.1~1kPa) had a higher probability of developing into neurons while those grown on stiffer substrates (20~80kPa) had a higher probability of becoming bone cells[11,12,41,42]. The large stiffness range of 0.7–100 MPa exhibited by the 4 fabricated material systems in this work allowed us to determine the role of the 3D scaffold stiffness on osteoblast behavior with regards to stress fibers concentration, cell adhesion, and mineral deposition. Fluorescence microscopy data revealed the presence of stress fibers (f-actin) and focal adhesions in SAOS-2 cells grown in mineralization media for 2 days on all 4 material systems. By measuring relative fluorescence intensity we observed that f-actin expression peaked on the most compliant nanolattices made from the hollow TiO_2 (material system (A)) and dropped by ~20% with increasing nanolattice stiffness (Fig. 3(iii)). This suggests that osteoblasts may be highly sensitive to substrate elasticity within a narrow substrate stiffness range of ~0.1–10MPa and virtually insensitive to it at higher stiffnesses. We postulate that when cells grow on a nanolattice with an elastic modulus larger than ~5MPa (Fig. 6(ii, iii)) the f-actin exerts forces that are larger than the tensile strength of the integrin-substrate bond, on the order of 100pN which causes its rupture. When this bond dissociates, the stiffness felt by the contracting actin filaments rapidly decreases and leads to f-actin depolymerization, which manifests itself as a decrease in fluorescence intensity.

Fluorescence results also revealed that the spatial distribution of the actin filaments appears to be a function of substrate stiffness. Figure 3(i) shows that the f-actin was uniformly distributed on the nanolattices of material system (A) and more confined to the nanolattice

beams on nanolattices made from material systems (B), (C) and (D). The excessive number of cells present on all nanolattices and the limitations in optical resolution of the instrument prevented us from drawing more quantitative conclusions about the spatial distribution of f-actin on the nanolattices. The relative fluorescence intensity of focal adhesion staining was within the error of the measurement for all material systems, which suggests their relative equivalence. Vinculin was observed along the nanolattice beams, which appear to provide anchor points for cell adhesion (Fig. 3(ii)). These observations may be explained by the functional differences between f-actin and focal adhesions. F-actin serves as an active mechanical element that constantly pulls on the substrate, its function has been reported to be strongly sensitive to substrate stiffness. Focal adhesions are passive mechanical elements that function as bridges for cell adhesion to the substrate regardless of its stiffness[48]. This functional difference may explain why the vinculin appears to be more sensitive to the availability of free surface area than to the substrate stiffness. All nanolattices in this work had a similar surface area available for cell attachment, which could explain the similarity in focal adhesion concentrations across material systems. Overlaying f-actin and vinculin fluorescence images allowed us to qualitatively observe a high degree of colocalization across all material systems (Fig. 3(v)); a signature that was previously observed when cells were grown in natural 3D environments derived from living tissues[24]. This finding suggests that the nanolattices used in this study may provide 3D platforms that adequately mimic natural microenvironments and elicit a cellular response comparable to that seen in vivo.

5.3 Cell Response: mineralization

After growing SAOS-2 cells on the nanolattices for 8 and 12 days in mineralization media, we observed that the scaffolds were fully coated with deposits of minerals and of organic matrix. SEM images shown in Fig. 4 reveal the presence of such deposits on all nanolattices that had two main morphologies: (1) organic cellular/proteinaceous matrix interspersed with ~50–100nm-wide filaments, which are consistent with collagen deposited by osteoblasts on 2D and 3D scaffolds[49] (Fig. 4(iii, iv, viii)), and (2) irregularly-shaped ~300–900nm-sized mineral aggregates which appear to be evenly distributed among the lattice beams (Fig. 4(v, vi); Fig. S3). These smaller formations appear to coalesce into larger, cauliflower-shaped aggregates, with dimensions of ~2–15μm. Similar deposits have been observed and identified as calcium phosphate species in our earlier work[50] (Fig. 4(v, vi, ix)).

Raman spectroscopy of the organic phase reveals the presence of several nucleic acids, fats and amino acids specifically proline and hydroxyproline, which are indicative of collagen (supplementary information, Fig. S6). Analysis of the larger, cauliflower-shaped deposits, indicates the presence of some form of bioapatite, which is the main mineral found in mature bone (Fig. 4(vii)). These findings suggest that SAOS-2 cells functionality was induced on the nanolattices. EDS analysis showed that the SAOS-2 cells which resided on the most compliant nanolattice (material system (A)) exhibited ~40% higher levels of Ca and P compared with those on all other scaffolds after growing in mineralization media for 8 days and ~10% higher after a growth period of 12 days. The relative amounts of Ca and P across material systems (B–D) after 8 and 12 days of cell growth remained relatively constant. After a cell growth period of 12 days, the difference in Ca and P between material system (A) and the other material systems (B–D) was much smaller (~10%) than that

observed after 8 days (~40%). These results suggest that: (1) more minerals are secreted onto the most compliant substrates and (2) deposition saturates after a certain amount of cell growth. The large reduction in the difference between mineral amounts between the most compliant system (A) and the other material systems also implies that rate of secretion is non-linear.

SEM images and EDS data also convey that the relative amounts of organic matrix quantified as the relative intensity of the C signal with respect to Ca and P decreased with time.

The intensity of carbon changed from being ~3 times greater than that of Ca and P on day 8 to approximately the same for all three elements on day 12 across all material systems. These results are consistent with the existing in-vivo models that postulate that the osteoblasts initially secrete an organic extracellular matrix, predominantly composed of collagen, which gets mineralized over time and forms several calcium-phosphate compounds.[51,52] This finding further suggests that the nanolattices may be able to evoke a cellular response similar to that observed in in-vivo studies, which render them a promising framework for future implants.

Elastic moduli of ~0.45 to 1MPa are typical of articular cartilage, which is the natural precursor of bone in mammals[53]. The results of this work suggest that utilizing 3D scaffolds with elastic moduli in that range may be promising in stimulating more efficient bone formation by mimicking embryonic development.

5.4 Concluding Remarks

We TPL to fabricate three-dimensional rigid polymer nanolattices whose strut dimensions were on the same order as osteoblasts' focal adhesions (~2μm) and pore sizes of 25μm. Some of these nanolattices were subsequently coated with thin conformal layers of Ti or W, and a final outer layer of 18nm-thick TiO_2 was deposited on all samples to ensure biocompatibility. Nanomechanical experiments on each type of nanolattice revealed their stiffnesses to range from ~0.7MPa to 100MPa. Osteoblast-like SAOS-2 cells were seeded on each type of nanolattice, and their mechanosensitive response was explored by tracking the intracellular f-actin and vinculin concentration after 2 days of cell culture.

Bone-like material that was deposited on the nanolattices by SAOS-2 cells was used as a cell functionality marker. Quantification of such deposits was performed via EDS after 8 and 12 days of cell growth in mineralization media.

These experiments revealed that the most compliant nanolattices, with the stiffness of 0.7 MPa, had a ~20% higher concentration of intracellular f-actin and ~40% more secreted Ca and P compared with all other nanolattices, where such cellular response was virtually indistinguishable.

We developed a simple phenomenological model that appears to capture the experimental observations. The underlying physical foundation of this model comes from incorporating the crucial role that integrins have in cell adhesion into well-established cell mechanics models.

The combination of the experiments and proposed theory suggest that the cell mineralization-inducing ability of 3D substrates is very sensitive to their structural stiffness and that optimal osteoblast functionality is attained on 3D substrates whose stiffness ranges from 0.7 to 3 MPa, similar to that of cartilage. These findings have significant implications for understanding the role that 3D scaffold stiffness plays in inducing mineralization and for introducing the nanolattices as promising platforms for new synthetic bone graft materials.

Supplementary Material

Refer to Web version on PubMed Central for supplementary material.

Acknowledgments

JRG and AM gratefully acknowledge the financial support of Amgen through AM's graduate fellowship.

References

1. Garellick G, et al. Arthroplasty Future Clinical and Economic Impact of Revision Total Hip and Knee Future Clinical and Economic Impact of Revision Total Hip and Knee Arthroplasty. J Bone Jt Surg Am. 2007; 89:144–151.
2. Roberts TT, Rosenbaum AJ. Bone grafts, bone substitutes and orthobiologics: the bridge between basic science and clinical advancements in fracture healing. Organogenesis. 2012; 8:114–24. [PubMed: 23247591]
3. Kilpadi KL, Chang PL, Bellis SL. Hydroxylapatite binds more serum proteins, purified integrins, and osteoblast precursor cells than titanium or steel. J Biomed Mater Res. 2001; 57:258–267. [PubMed: 11484189]
4. Niinomi M, Nakai M. Titanium-based biomaterials for preventing stress shielding between implant devices and bone. Int J Biomater. 2011; 2011
5. Hutmacher DW. Scaffolds in tissue engineering bone and cartilage. Biomaterials. 2000; 21:2529–2543. [PubMed: 11071603]
6. Huiskes R. Stress shielding and bone resorption in THA: clinical versus computer-simulation studies. Acta Orthop Belg. 1993; 59(Suppl 1):118–129. [PubMed: 8116386]
7. Nagels J, Stokdijk M, Rozing PM. Stress shielding and bone resorption in shoulder arthroplasty. J Shoulder Elb Surg. 2003; 12:35–39.
8. Engler AJ, Sen S, Sweeney HL, Discher DE. Matrix Elasticity Directs Stem Cell Lineage Specification. Cell. 2006; 126:677–689. [PubMed: 16923388]
9. Murphy WL, McDevitt TC, Engler AJ. Materials as stem cell regulators. Nat Mater. 2014; 13:547–557. [PubMed: 24845994]
10. Discher DE, Janmey P, Wang YL. Tissue cells feel and respond to the stiffness of their substrate. Science. 2005; 310:1139–43. [PubMed: 16293750]
11. Pedersen JA, Swartz MA. Mechanobiology in the third dimension. Ann Biomed Eng. 2005; 33:1469–1490. [PubMed: 16341917]
12. Wu S, Liu X, Yeung KWK, Liu C, Yang X. Biomimetic porous scaffolds for bone tissue engineering. Mater Sci Eng R Reports. 2014; 80:1–36.
13. Cui Y, et al. The nanocomposite scaffold of poly(lactide-co-glycolide) and hydroxyapatite surface-grafted with l-lactic acid oligomer for bone repair. Acta Biomater. 2009; 5:2680–2692. [PubMed: 19376759]
14. Fu Q, Saiz E, Tomsia AP. Bioinspired strong and highly porous glass scaffolds. Adv Funct Mater. 2011; 21:1058–1063. [PubMed: 21544222]
15. Wagoner Johnson AJ, Herschler BA. A review of the mechanical behavior of CaP and CaP/polymer composites for applications in bone replacement and repair. Acta Biomater. 2011; 7:16–30. [PubMed: 20655397]

16. Karageorgiou V, Kaplan D. Porosity of 3D biomaterial scaffolds and osteogenesis. Biomaterials. 2005; 26:5474–5491. [PubMed: 15860204]
17. Fu Q, Saiz E, Rahaman MN, Tomsia AP. Bioactive glass scaffolds for bone tissue engineering: State of the art and future perspectives. Mater Sci Eng C. 2011; 31:1245–1256.
18. Raimondi MT, et al. Three-dimensional structural niches engineered via two-photon laser polymerization promote stem cell homing. Acta Biomater. 2013; 9:4579–4584. [PubMed: 22922332]
19. Maggi A, Allen J, Desai T, Greer JR. Osteogenic cell functionality on 3-dimensional nano-scaffolds with varying stiffness. Extrem Mech Lett. 2017; 13:1–9.
20. Harley BAC, et al. Microarchitecture of three-dimensional scaffolds influences cell migration behavior via junction interactions. Biophys J. 2008; 95:4013–4024. [PubMed: 18621811]
21. Tayalia BP, Mendonca CR, Baldacchini T, Mooney DJ, Mazur E. 3D Cell-Migration Studies using Two-Photon Engineered Polymer Scaffolds **. 2008; :4494–4498. DOI: 10.1002/adma.200801319
22. Jakus AE, et al. Hyperelastic ‘bone’: A highly versatile, growth factor–free, osteoregenerative, scalable, and surgically friendly biomaterial. Sci Transl Med. 2016; 8:358ra127–358ra127.
23. Tayalia P, Mendonca CR, Baldacchini T, Mooney DJ, Mazur E. 3D cell-migration studies using two-photon engineered polymer scaffolds. Adv Mater. 2008; 20:4494–4498.
24. Cukierman E. Taking Cell-Matrix Adhesions to the Third Dimension. Science (80-). 2001; 294:1708–1712.
25. Chen G, Dong C, Yang L, Lv Y. 3D Sca ff olds with Different Stiffness but the Same Microstructure for Bone Tissue Engineering. 2015; doi: 10.1021/acsami.5b02662
26. Gibson LJ, Ashby MF. Cellular solids: Structure and properties. Materials Science and Engineering: A. 1990; 123
27. Deshpande VS, Ashby MF, Fleck NA. Foam topology: Bending versus stretching dominated architectures. Acta Mater. 2001; 49:1035–1040.
28. Ashby MF. The properties of foams and lattices. Philos Trans A Math Phys Eng Sci. 2006; 364:15–30. [PubMed: 18272451]
29. Gibson LJ. Biomechanics of cellular solids. J Biomech. 2005; 38:377–399. [PubMed: 15652536]
30. Jaafar IH, et al. Improving fluorescence imaging of biological cells on biomedical polymers. Acta Biomater. 2011; 7:1588–1598. [PubMed: 21145439]
31. Meza LR, Greer JR. Mechanical characterization of hollow ceramic nanolattices. J Mater Sci. 2014; 49:2496–2508.
32. Papka SD, Kyriakides S. In-plane compressive response and crushing of honeycomb. J Mech Phys Solids. 1994; 42:1499–1532.
33. Ingber DE. TENSEGRITY: THE ARCHITECTURAL BASIS OF CELLULAR. 1997
34. Wang N, Butler JPP, Ingber DEE. Mechanotransduction across the cell surface and through the cytoskeleton. Science. 1993; 260:1124–1127. [PubMed: 7684161]
35. Rodriguez ML, McGarry PJ, Sniadecki NJ. Review on cell mechanics: Experimental and modeling approaches. Appl Mech Rev. 2013; 65:060801.
36. McGarry JG, Prendergast PJ. A three-dimensional finite element model of an adherent eukaryotic cell. Eur Cell Mater. 2004; 7:27–33. discussion 33–34. [PubMed: 15095253]
37. He S, Su Y, Ji B, Gao H. Some basic questions on mechanosensing in cell-substrate interaction. J Mech Phys Solids. 2014; 70:116–135.
38. Milo R, Phillips R. Cell Biology By the Numbers. Current opinion in plant biology. 2014; doi: 10.1016/j.pbi.2009.10.009
39. De Santis G, et al. How can cells sense the elasticity of a substrate? an analysis using a cell tensegrity model. Eur Cells Mater. 2011; 22:202–213.
40. Gefen A. Cellular and biomolecular mechanics and mechanobiology. Computer Methods in Biomechanics and Biomedical Engineering. 2012; doi: 10.1080/10255842.2012.705081
41. Li F, Redick SD, Erickson HP, Moy VT. Force measurements of the alpha5beta1 integrin-fibronectin interaction. Biophys J. 2003; 84:1252–1262. [PubMed: 12547805]
42. Cavalcanti-Adam EA, et al. Cell spreading and focal adhesion dynamics are regulated by spacing of integrin ligands. Biophys J. 2007; 92:2964–74. [PubMed: 17277192]

43. Meza LR, Das S, Greer JR. Strong, lightweight, and recoverable three-dimensional ceramic nanolattices. 2014; doi: 10.1126/science.1255908
44. Bauer J, Hengsbach S, Tesari I, Schwaiger R, Kraft O. High-strength cellular ceramic composites with 3D microarchitecture. Proc Natl Acad Sci U S A. 2014; 111:2453–8. [PubMed: 24550268]
45. Meza LR, et al. Resilient 3D hierarchical architected metamaterials. Proc Natl Acad Sci U S A. 2015; 112:11502–7. [PubMed: 26330605]
46. Ozdemir T, Xu LC, Siedlecki C, Brown JL. Substrate curvature sensing through Myosin IIa upregulates early osteogenesis. Integr Biol (Camb). 2013; 5:1407–16. [PubMed: 24104522]
47. Mrksich M, Huang S, Whitesides GM, Ingber DE. Geometric control of cell life and death. 1997:276.
48. Yeung T, et al. Effects of substrate stiffness on cell morphology, cytoskeletal structure, and adhesion. Cell Motil Cytoskeleton. 2005; 60:24–34. [PubMed: 15573414]
49. Verma D, Katti KS, Katti DR. Osteoblast adhesion, proliferation and growth on polyelectrolyte complex-hydroxyapatite nanocomposites. Philos Trans A Math Phys Eng Sci. 2010; 368:2083–97. [PubMed: 20308116]
50. Rezwan K, Chen QZ, Blaker JJ, Boccaccini AR. Biodegradable and bioactive porous polymer/inorganic composite scaffolds for bone tissue engineering. Biomaterials. 2006; 27:3413–3431. [PubMed: 16504284]
51. Owen TA, et al. Progressive development of the rat osteoblast phenotype in vitro: Reciprocal relationships in expression of genes associated with osteoblast proliferation and differentiation during formation of the bone extracellular matrix. J Cell Physiol. 1990; 143:420–430. [PubMed: 1694181]
52. Gilbert, SF. Developmental Biology. Osteogenesis: The Development of Bones. Dev Biol. 62000. http://www.ncbi.nlm.nih.gov/books/NBK10056/doi:10:0-87893-243-7
53. Mansour JM. Biomechanics of Cartilage. Kinesiol Mech pathomechanics Hum Mov. 2009; :66–79. DOI: 10.1002/art.23548

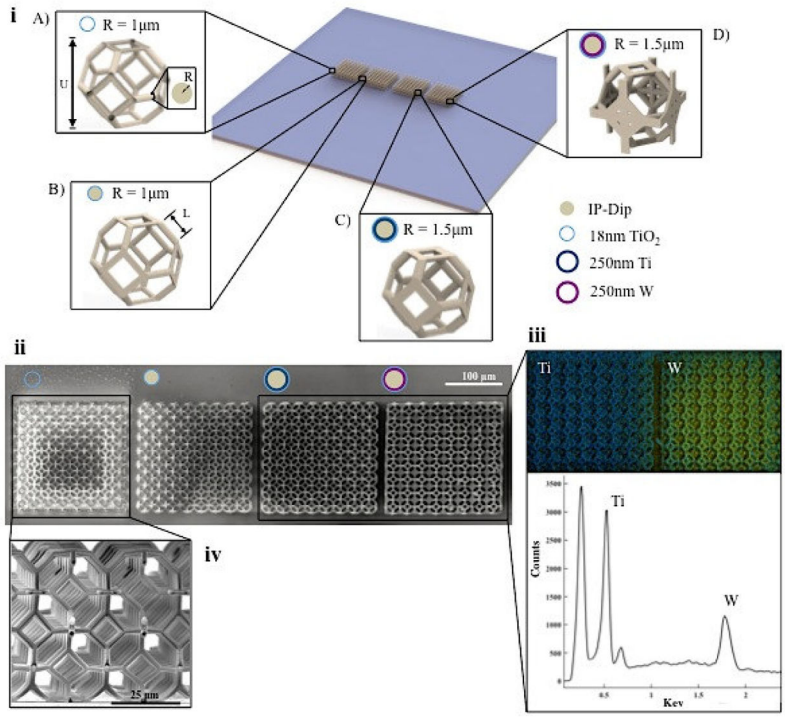

Figure 1. Design and Fabrication of the Nanolattices

(i) Computer-aided design of the sample showing the four types of nanolattices that were tested. All nanolattices had tetrakaidecahedral unit cells of length (U) = 25μm and a beam radius (R), which varied from 1 to 1.5μm. The insets show a zoomed-in view of the unit cells that comprise each type of nanolattice: (A) hollow with an 18nm-thick TiO_2 wall. (B) IP-Dip-core coated with 18nm-thick layer of TiO_2. (C) IP-Dip-core coated with ~250nm-thick layer of Ti and 18nm-thick layer of TiO_2. (D) IP-Dip-core coated with ~250nm-thick layer of W and 18nm-thick layer of TiO_2. (**ii)** Top SEM view of the fabricated samples. (**iii)** EDS map and spectrum that shows the composition of the W and Ti nanolattices (material systems C and D). (**iv)** A zoomed-in side SEM view of the hollow TiO2 nanolattice (material system (A)).

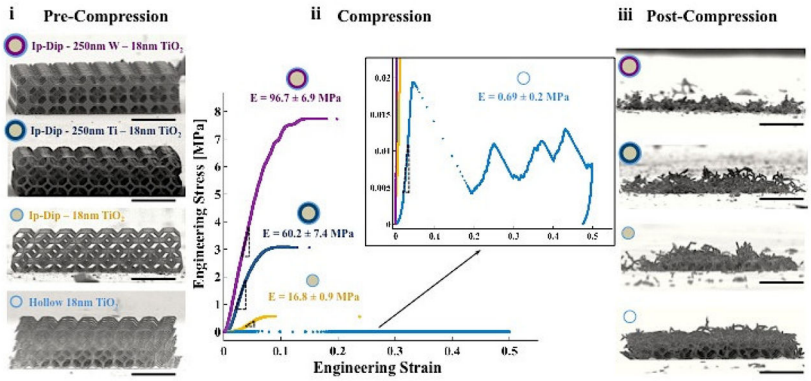

Figure 2. Uniaxial compression experiments

(i) SEM images of representative as-fabricated samples from each material system. The circles in the top left corner of each image represent a schematic of the beam cross section for each material system (not to scale). **(ii)** Representative stress-strain response to quasi-static uniaxial compression of each material system. The inset shows a zoomed-in view of the compression of the hollow nanolattice (wall thickness = 18nm TiO_2). **(iii)** SEM images of the same samples after compression. All samples from material systems B, C, and D underwent brittle failure, the hollow nanolattice (A) (bottom image) experienced localized Euler beam buckling and some residual recovery. Scale bars in each SEM image represent 50μm.

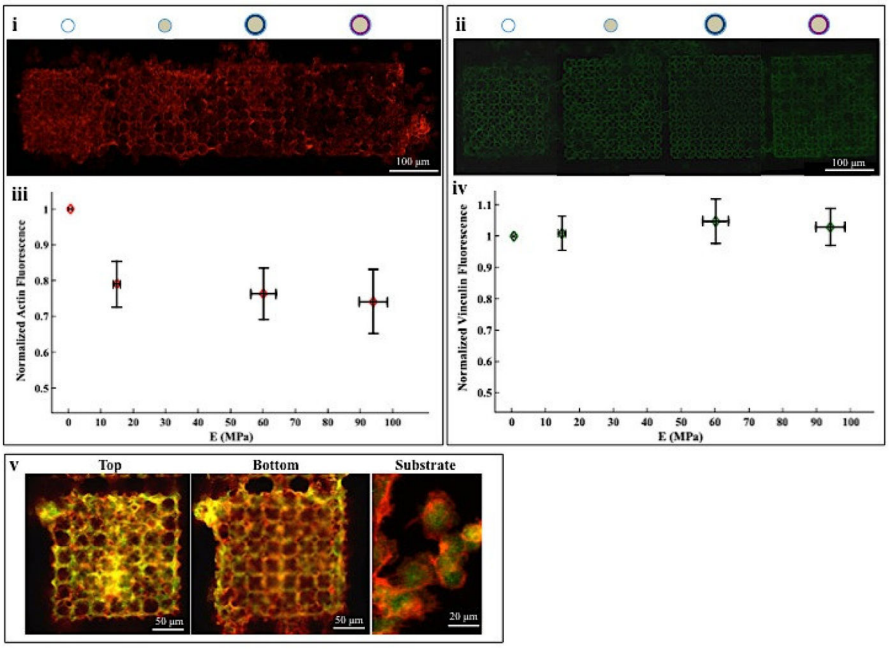

Figure 3. Fluorescence microscopy images and quantitative analysis

(i) Z-stack projections of confocal images of SAOS-2 cells grown on the nanolattices for 2 days that show actin filaments stained with Phalloidin and **(ii)** focal adhesions stained with anti-vinculin antibodies; the material system is represented by the schematic circle on top of the corresponding nanolattice. Relative amounts of f-actin **(iii)** and focal adhesions **(iv)** as a function of nanolattice stiffness. Fluorescence data was normalized by the intensity of the most compliant material system (A). Horizontal error bars represent standard deviation in nanolattice elastic moduli and vertical error bars represent standard error in fluorescence measurements. **(v)** Merging of the red and green channels shows higher levels of co-localization (yellow) on the nanolattices compared to the surrounding flat substrate.

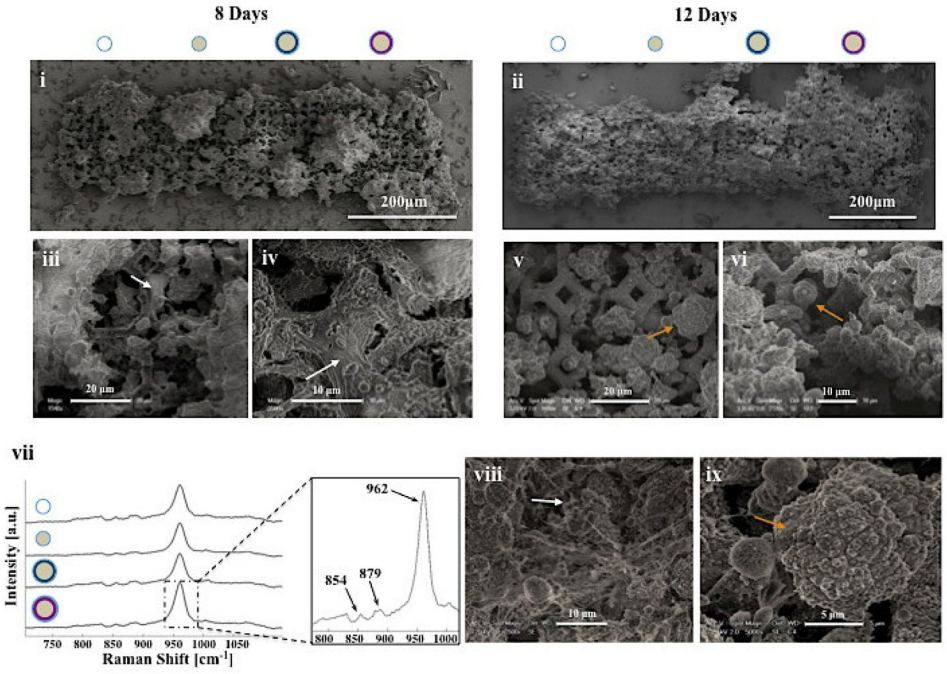

Figure 4. SEM images of the SAOS-2 cells' products after growing for 8 and 12 days in mineralization media

(i, ii) Top-down SEM images of the samples after 8 days **(i)** and 12 days **(ii)** of growth. Circles above the images represent a schematic of the individual beam cross-sections for each material system. **(iii, iv)** Zoomed-in SEM images that reveal large amounts of organic material (white arrows) grown on the nanolattice after 8 days. These deposits were found across all material systems. **(v, vi)** Zoomed-in SEM images showing large amounts of mineral formations (orange arrows) on the nanolattices after 12 days. These aggregates were found across all material systems**. (vii)** Raman spectroscopy analysis of SAOS-2 products after 12 days of growth. Spectra collected from all material systems revealed the presence of bioapatite (962 cm^{-1}) and collagen molecules (854 cm^{-1}, 879 cm^{-1}). **(viii)** SEM image of the organic phase that shows the presence of filamentous features with diameters of 75 ± 32nm, consistent with the size of collagen fibrils. **(ix)** SEM image of a mineral aggregate that most probably corresponds to bioapatite.

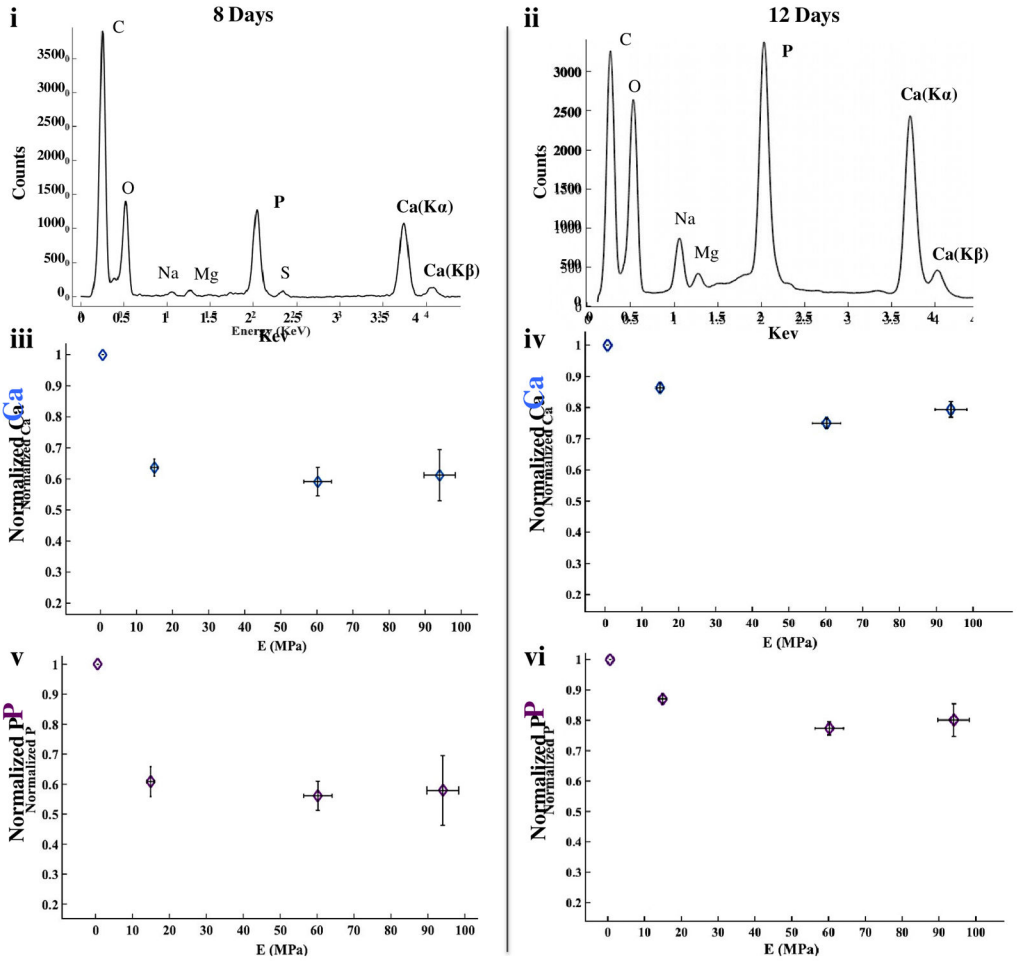

Figure 5. EDS spectra and quantification of Ca and P secreted by the SAOS-2 cells

(i, ii) Representative EDS spectra after growing SAOS-2 cells for 8 days **(i)** and 12 days **(ii)** in mineralization media. **(iii–vi)** Relative intensity of Ca (**iii, iv**) and P (**v, vi**) after 8 days **(iii, v)** and 12 days **(iv, vi). (v, vi)** Horizontal error bars represent the standard deviation in elastic moduli measured over 4 samples and vertical error bars represent the standard error in the intensity of Ca and P obtained from EDS spectra of 3 chips per time point. In each plot, Ca and P concentrations were normalized by their relative amounts on the most compliant material system (A).

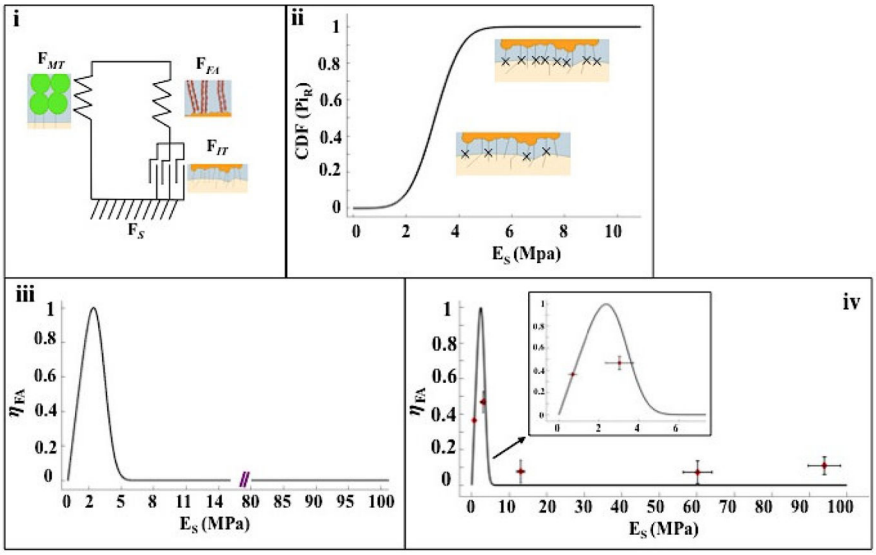

Figure 6. Substrate-dependent f-actin activation model

(i) Model phenomenology: F_{MT} represents the force exerted by microtubules (green), F_{AF} represents the force exerted by f-actin filaments (red) and F_{IT} represents the force exerted by integrins (black). F_S represents the resistive force of the substrate. Microtubules, f-actin and the substrate were modeled as elastic solid springs; the integrins were modeled as sliders. **(ii)** Cumulative distribution function (CDF(Pi_R)) of a cluster of integrins per micron squared as a function of substrate elasticity that shows more integrin-substrate bonds breaking as stiffness increases. **(iii**) Model predictions of f-actin concentration change (η_{FA}) as a function of substrate stiffness. **(iv)** F-actin activation factor, η_{FA}, as a function of the structural stiffness of the substrate. Solid line represents theoretical predictions, open diamond symbols represent experimental data.

Table I

Elastic modulus, E*, and compressive strength, σ_f, of each material system measured via uniaxial quasi-static compression. Error was calculated by taking the standard deviation from 4 data points gathered per material system.

System	E* (Mpa)	σ_f (Mpa)
A	0.69 ± 0.2	0.019 ± 0.003
B	16.8 ± 0.9	0.45 ± 0.01
C	60.2 ± 7.4	1.78 ± 0.28
D	96.7 ± 6.9	4.53 ± 0.7